A&A 567, A34 (2014)
DOI: 10.1051/0004-6361/201323335

Astronomy & Astrophysics

The Gemini NICI planet-finding campaign: The offset ring of HR 4796 A⋆,⋆⋆

Zahed Wahhaj[1], Michael C. Liu[2], Beth A. Biller[3], Eric L. Nielsen[2], Thomas L. Hayward[4], Marc Kuchner[5], Laird M. Close[6], Mark Chun[2], Christ Ftaclas[2], and Douglas W. Toomey[7]

[1] European Southern Observatory, Alonso de Córdova 3107, Vitacura, Casilla 19001 Santiago, Chile
[2] Institute for Astronomy, University of Hawaii, 2680 Woodlawn Drive, Honolulu HI 96822, USA
[3] Institute for Astronomy, The University of Edinburgh, Royal Observatory, Blackford Hill, Edinburgh EH9 3HJ, UK
[4] Gemini Observatory, Southern Operations Center, c/o AURA, Casilla 603 La Serena, Chile
[5] NASA Goddard Space Flight Center, Exoplanets and Stellar Astrophysics Laboratory, Greenbelt MD 20771, USA
[6] Steward Observatory, University of Arizona, 933 North Cherry Avenue, Tucson AZ 85721, USA
[7] Mauna Kea Infrared, LLC, 21 Pookela St., Hilo HI 96720, USA

Received 25 December 2013 / Accepted 23 April 2014

ABSTRACT

We present J, H, CH_4 short (1.578 μm), CH_4 long (1.652 μm) and K_s-band images of the dust ring around the 10 Myr old star HR 4796 A obtained using the Near Infrared Coronagraphic Imager (NICI) on the Gemini-South 8.1 m Telescope. Our images clearly show for the first time the position of the star relative to its circumstellar ring thanks to NICI's translucent focal plane occulting mask. We employ a Bayesian Markov chain Monte Carlo method to constrain the offset vector between the two. The resulting probability distribution shows that the ring center is offset from the star by 16.7 ± 1.3 milliarcseconds along a position angle of $26 \pm 3°$, along the PA of the ring, $26.47 \pm 0.04°$. We find that the size of this offset is not large enough to explain the brightness asymmetry of the ring. The ring is measured to have mostly red reflectivity across the JHK_s filters, which seems to indicate micron-sized grains. Just like Neptune's 3:2 and 2:1 mean-motion resonances delineate the inner and outer edges of the classical Kuiper belt, we find that the radial extent of the HR 4796 A and the Fomalhaut rings could correspond to the 3:2 and 2:1 mean-motion resonances of hypothetical planets at 54.7 AU and 97.7 AU in the two systems, respectively. A planet orbiting HR 4796 A at 54.7 AU would have to be less massive than 1.6 M_{Jup} so as not to widen the ring too much by stirring.

Key words. planet-disk interactions – infrared: planetary systems – instrumentation: adaptive optics – Kuiper belt: general – techniques: high angular resolution – methods: statistical

1. Introduction

Debris disks are composed of dust produced by collisions between planetesimals orbiting stars at age $\gtrsim$10 Myr (e.g., Backman & Paresce 1993; Wyatt 2008). Since the first image of a debris disk around β Pictoris (Smith & Terrile 1984), more than three dozen debris disks have been resolved in the optical, infrared and submillimeter[1]. Most of these disks exhibit asymmetries which are difficult to explain without invoking a dynamical perturber, for example a planet (Wyatt 2008). In the case of β Pictoris, there is now evidence that the recently discovered planet (Lagrange et al. 2009, 2010), may be directly responsible for one of these asymmetries, a warp in the disk (Lagrange et al. 2012; Heap et al. 2000; Mouillet et al. 1997). Moreover, many of the directly imaged planets have been found around A stars with debris disks (Marois et al. 2010; Lagrange et al. 2010; Kalas et al. 2013; Rameau et al. 2013), which suggests that these systems at one time possessed massive primordial disks. Thus debris disks may indicate the presence of planets in two ways: (1) by their morphology and (2) by their presence alone.

The debris ring around the young (8−10 Myr; Stauffer et al. 1995) A0 star HR 4796 A has two asymmetries: (1) a brightening of its north-east ansa with respect to its south-west ansa (Koerner et al. 1998; Wyatt et al. 1999; Schneider et al. 1999); and (2) a possible offset of the ring center from the star (Schneider et al. 2009; Thalmann et al. 2011). Wyatt et al. (1999) have argued that these two phenomenon may be related to the greater exposure of the ring to stellar radiation at the pericenter. However, the offset may also be caused by the stellar companion (M2.5V; Barrado Y Navascués 2006) at 7.86″ (Epoch UT April 6, 2012) which has a position angle (PA) similar ($45° \pm 1+180°$) to that of the ring (Jura et al. 1993). The ring has a PA of $26.01 \pm 0.16°$ and an inclination to the line of sight of $75.88 \pm 0.16°$ ($\approx$14° from edge-on; Schneider et al. 2009). It has been suggested that the narrowness of the ring could be due to inner and outer planetary companions (Wyatt et al. 1999). Any sharp outer cutoff cannot be explained by the stellar companion alone (Thébault et al. 2010). On the other hand, it appears that the outer edge of the ring may have a long tenuous tail (Wahhaj et al. 2005; Thalmann et al. 2011). However, the

⋆ Based on observations obtained at the Gemini Observatory, which is operated by the Association of Universities for Research in Astronomy, Inc., under a cooperative agreement with the NSF on behalf of the Gemini partnership: the National Science Foundation (United States), the Science and Technology Facilities Council (United Kingdom), the National Research Council (Canada), CONICYT (Chile), the Australian Research Council (Australia), Ministério da Ciência e Tecnologia (Brazil) and Ministerio de Ciencia, Tecnología e Innovación Productiva (Argentina).

⋆⋆ Tables 5 and 6 are available in electronic form at http://www.aanda.org

[1] The catalog of circumstellar disks is available at http://www.circumstellardisks.org/

Table 1. Opacity of the 0.32″ NICI focal plane mask (Wahhaj et al. 2013a).

Filters	Opacity (mag)	Uncertainty (mag)
J	6.37	0.12
H	5.94	0.05
K_s	5.70	0.09
CH_4S	6.385	0.029
CH_4L	6.204	0.048

narrow "streamers" emanating from the outer edges of the ring as reported in Thalmann et al. (2011) appear to be an artifact from image processing that is only significant in angular differential observations with insufficient total sky rotation (Lagrange et al. 2012; Milli et al. 2012). Wahhaj et al. (2005) found that combined modeling of the Keck mid-infrared (MIR) images and HST near-infrared (NIR) images required the existence of a wide ring (extending from 0.7″ to 1.9″) which was 10 times more tenuous than the narrow ring with radius 1.05″ (76.4 AU for a distance of 72.78 pc; van Leeuwen 2007). The wide ring, with smaller and lower albedo grains than the narrow ring, could be interpreted as dust being blown away by radiation pressure. The source of the blow-out dust would mainly be planetesimals in the narrow ring, but also could include a lower density population interior to it.

In this paper, we present images of the HR 4796 A ring taken with the Near Infrared Coronagraphic Imager (NICI) at the 8-m Gemini South Telescope in the JHK_s and two methane bands. These images clearly show, for the first time, the positions of the star and the ring so that any relative shift can be measured very precisely. The ring ansae asymmetry is also detected in all five bands, and thus confirmed unambiguously here. Lastly, we review the possible causes of these two asymmetries.

2. Observation

We observed HR 4796 A on UT 2009 January 14 and UT 2012 April 6 and 7 with NICI (Chun et al. 2008) as part of the Gemini NICI Planet-Finding Campaign on the Gemini-South 8.1 m Telescope (Liu et al. 2010; Wahhaj et al. 2013b; Nielsen et al. 2013; Biller et al. 2013). The star was observed in Angular Difference Imaging (ADI; Liu 2004; Marois et al. 2006) mode, with two different filters in NICI's two cameras. On 2009 January 14, we used the CH_4S (λ = 1.578 μm) and CH_4L (λ = 1.652 μm) moderate-bandwidth ($\Delta\lambda/\lambda$ = 4%) filters with a 50/50 beamsplitter sending light to the two cameras (plate scales 17.96 ± 0.01 mas/pixel for CH_4S and 17.94 ± 0.01 mas/pixel for CH_4L), which were read out simultaneously. The integration time per image was 1 minute. The star was placed behind the semi-transparent (0.28% central transmission) focal plane mask with a half-transmission radius of 0.32″. The central opacities for the various filters are provided in Table 1. These were measured by observing a pair of stars 4.2″ apart of known flux ratio from the 2MASS catalog, as described in Wahhaj et al. (2011).

Thanks to the focal plane mask, HR 4796 A was imaged without saturation so that its position with respect to the debris ring can be measured very precisely. On 2012 April 6, we imaged simultaneously in the H and K_s bands and on April 7, we imaged only in the J band, sending all the light to one camera by replacing the dichroic with a mirror. In the April 6 observations, the star was only lightly saturated, exhibiting no obvious change in the point-spread-function (PSF) shape. The total number of images taken and the total sky rotation obtained in ADI mode at each epoch are presented in Table 2. The smearing of the sky due to ADI mode during an individual image was <1.5° for all observations, or <0.5 FWHM of the NICI PSF at 1″.

3. Data reduction

We aim to estimate the center of the HR 4796 A ring and compare it to the location of the star. For this purpose we focus only on the brightest parts of the ring. The brightness decreases quickly on either side of the bright rim. Thus, we use the point-source recovery ADI pipeline as described in Wahhaj et al. (2013a), since it is most successful at removing starlight and isolating the brightest parts of the ring. The steps of the pipeline are:

1. Do basic reduction: apply flatfield, distortion and position angle corrections.
2. Find centroids and apply image filters to the images.
3. Subtract the median of the stack from the individual difference images (ADI subtraction).
4. De-rotate and stack the images.

In this pipeline, we filter the images to remove emission at spatial scales that are less than half or more than twice the full width at half maximum (FWHM) of the NICI H-band PSF (≈3 pixels or 54 mas). Thus ring features which are much larger or smaller than the NICI PSF are not present in the reduced image.

In step 3 of the pipeline, the median image is fit to each science image to minimize the root mean square (rms) in an annulus in the difference image. The fit is performed using a simplex-downhill method which searches for optimum intensity scalings and horizontal and vertical shifts. The annulus used for the fit has inner and outer radii of 0.6″ and 0.8″, respectively.

The subtraction of the reference PSF in step 3 causes different amounts of flux to be lost from different parts of the ring, potentially changing its morphology. However, since we have 24−81° of sky rotation (see Table 2), the image of the ring ansae (radius 1″) moves over more than 20 pixels on the detector as the science images are obtained. As a result, the contribution from the ring to the median combination of the stack and thus to the PSF subtraction is negligible. The reduced images are shown in Fig. 1.

4. Analysis

We have reduced images in five filters of the bright rim of the HR 4796 A ring, two obtained in January 2009 (CH_4 short and CH_4 long) and three in April 2012 (JHK_s). In these images, both the location of the star and the ring are captured at a resolution of 54 mas. In this section, we model the rim as a ring with a Gaussian profile, viewed at some PA and inclination, with an offset of the ring center from the star.

We use three different methods to determine the offset of the ring center relative to the star:

1. Radial profiles along different PAs toward the NE and SW ansae to determine the maximum separations of the ring in the two directions (without a ring model).
2. Bayesian MCMC analysis to produce probability distributions for the ring offset in RA and Dec.
3. Bayesian MCMC analysis like method 2, but also modeling the self-subtraction of the ring.

Table 2. NICI observations of HR 4796 A.

UT date	Filters	N_{frames}	Rotation (°)	Comments
2012 April 7	J	66	73	Unsaturated star
2012 April 6	$H + K$	74	81	Lightly saturated star
2009 January 14	CH_4 short + CH_4 long (4%)	49	24	Unsaturated star
2009 January 14	H	20	22	Saturated star

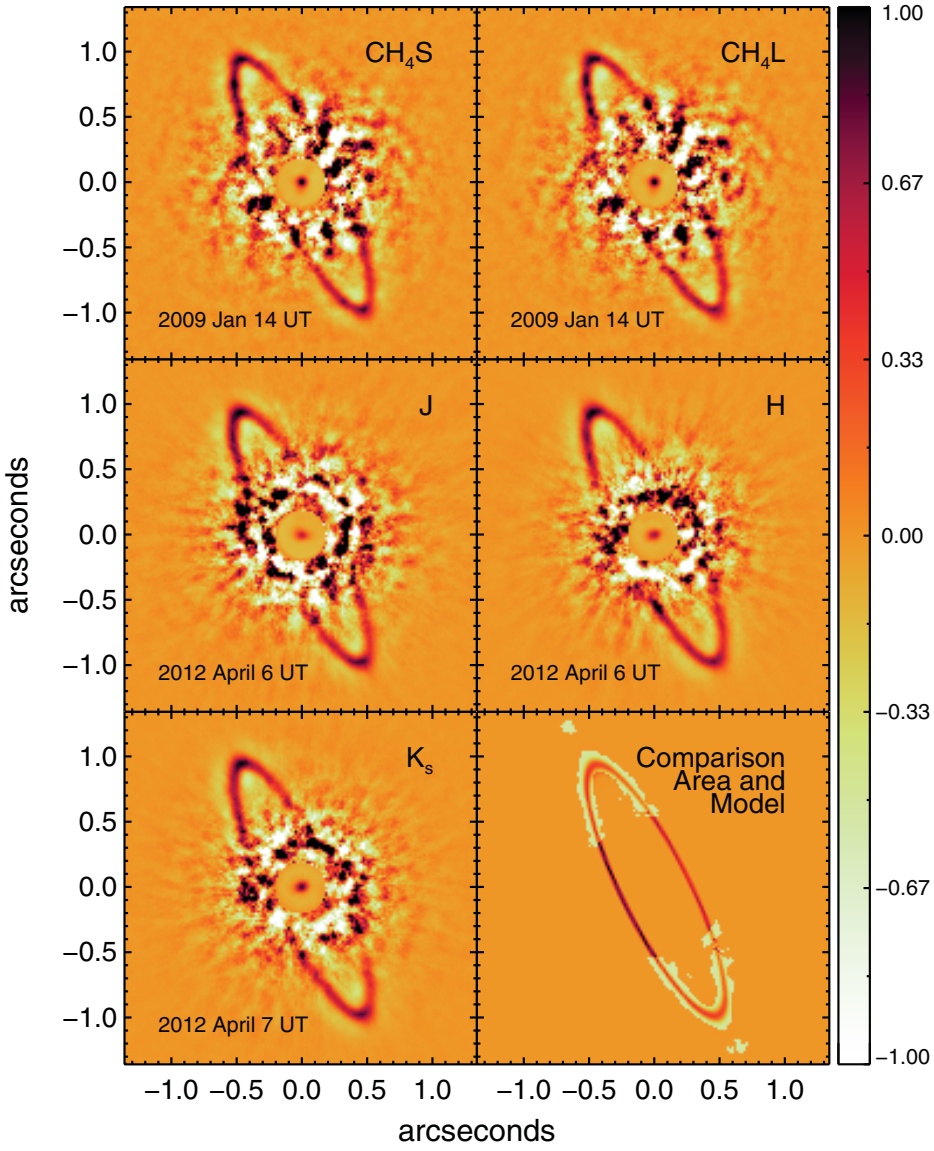

Fig. 1. Unsaturated images of HR 4796 A, with both the star and dust ring detected with high astrometric precision. Reduced images from five filters taken in two epochs are shown. The black spot in the centers of the panels show the star (unsaturated in J, CH_4 short and CH_4 long; see Table 2). The intensities within 180 mas of the star have been divided by 100 to clearly show the unsaturated stellar peak. The reductions were done using a point-source recovery pipeline, which yields a higher fidelity image of the bright rim of the HR 4796 A disk. The *last panel to the bottom right* is the best-fit model to the K_s-band image with the model and data comparison region highlighted (by subtracting 0.5 from the region's pixel values). The color bar to the right gives the normalized pixel intensities in linear scale.

4.1. Method 1: radial profiles

We first study the radial profiles starting at the stellar position, pointed along several PAs towards the ring ansa, at increments of 0.1°. Since the star is detected at very high signal to noise and is unsaturated, the uncertainty in its location is only 0.2 mas and is limited by the centroiding algorithm and the pixel size (Wahhaj et al. 2013a). For each of these profiles, we estimate by cubic interpolation the projected separation of the brightest peak. Figure 2 shows these projected separations for the five filters. It is clear the NE ansae is consistently found to be closer to the star. Moreover, the peaks in the NE and SW ansae are found to lie along a straight line, giving credence to the method.

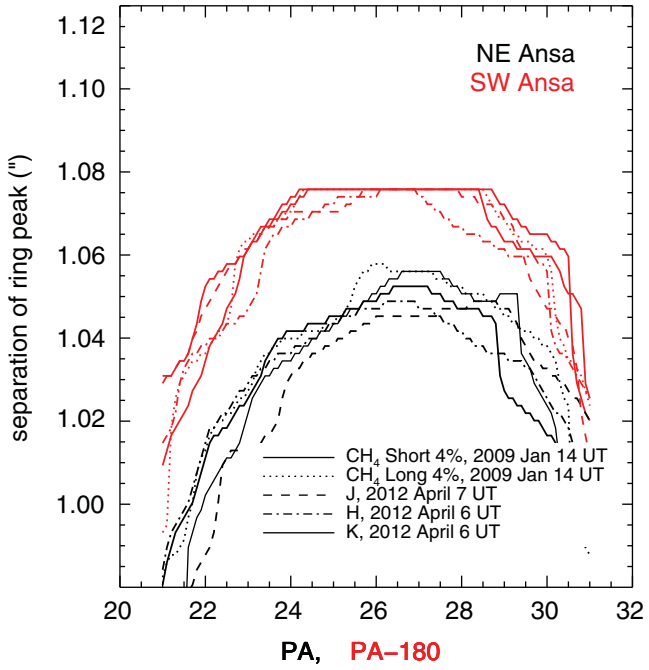

Fig. 2. Line cuts taken from the stellar position along different PAs towards the ring ansae. The PA towards the SW ansa, shown in red, has had 180° subtracted from it for easy comparison with the NE ansa (shown in black). This illustrates that the NE and SW peaks are not equally separated from the star. In other words, the ring is offset from the star.

4.2. Method 2: Bayesian MCMC fitting

To quantify the ring offset, we compare a ring model to our NICI images using the χ^2 statistic. To avoid the effect of regions where the ring is faint compared to residuals from the PSF subtraction, we mask out regions not close to the ring ansae and exclude them from our fitting. Regions within 0.55″ of the star are also not included in the comparisons. The ring is known to be inclined to the line of sight at an angle of $75.88 \pm 0.16°$ (Schneider et al. 2009). We use this inclination to also exclude all regions with projected separations outside the 0.8″ to 1.5″ range. Furthermore, regions with negative emission which result from filtering the images are also excluded from the comparison, since they are not physical. The comparison region is shown together with the model for the K_s-band in Fig. 1. For the K_s-band, a total of 1041 pixels or approximately 147 resolutions elements make up the comparison region. The region has a similar size in the other bands.

For reasonable χ^2 statistics, we need a good estimate of the noise in the images. In order to remove all spatial features much larger than two pixels, we convolve the data with a Gaussian kernel of 2 pixel FWHM and subtract the result from the data. We then take the standard deviation of the pixel values in the fitting region (defined above) as the noise when calculating χ^2. This standard deviation is 8 times larger than that of a Gaussian distribution with the same FWHM, indicating a distribution with long tails. Indeed the ring emission is still contributing to the standard deviation as seen in the residual image. However, it is preferable to over estimate the noise since then the final constraints we obtain will be conservative.

The χ^2 statistic is given by

$$\chi^2 = \sum_{\text{pixels}} \frac{(\text{Data} - \text{Model})^2}{\text{noise}^2}. \quad (1)$$

The brightness of the ring $B(r)$ is modeled as a circular annulus of mean radius, r_0, with a radial brightness profile described by a Gaussian of width σ

$$B(r) = B_0 e^{-(r_0 - r)^2/2\sigma^2}. \quad (2)$$

The additional parameters of the model are the inclination, PA, and ring center offsets, ΔRA and ΔDec, totalling seven parameters which completely describe the model. As a starting point for the Bayesian MCMC computations, we find the best-fit parameters using the simplex-downhill IDL routine, AMOEBA (e.g., Press et al. 1992).

We use a Metropolis-Hastings Markov chain Monte Carlo (MCMC) method to calculate the posterior probabilities for the seven ring parameters. According to Bayes's theorem, the probability of a model given the data is

$$P(\text{Model}|\text{Data}) = P(\text{Data}|\text{Model}) \frac{P(\text{Model})}{P(\text{Data})}.$$

Since we do not intend to include prior information about the data or the model, we set $P(\text{Model})/P(\text{Data}) = 1$. The probability of the data given the model, $P(\text{Data}|\text{Model})$, is given by $e^{-\chi^2/2}$.

We start at a given point in the seven-dimensional parameter space of models. Next, a trial jump to a new point in the parameter space is evaluated on the basis of its probability relative to the current point. Whether the jump to the new location is accepted is decided by the Metropolis-Hastings measure (e.g., for a full description see Gregory 2005). If the trial jump is accepted, the new location becomes the current location. Otherwise, the current location stays the same. In either case, a new trial jump is considered. This process is repeated until we converge to an equilibrium. The entire set of locations at each step gives the posterior probability distribution for the seven model parameters (Metropolis et al. 1953).

The trial jump is given by a seven-dimensional vector chosen randomly from a seven-dimensional Gaussian distribution with appropriate standard deviations along each dimension. These standard deviations are chosen so that the trial jump is accepted at a rate between 25% and 75%. If the accepted rate is not within this range, then the solution will take too long to converge.

For our images in each of the five filters, we compare 2 million models to the data using this MCMC method. The probability distribution for each of the seven parameters is given by the histogram of the 1D array (a column of length 2 million) corresponding to the desired model parameter. The probability distributions from the first and second halves of the MCMC run are compared to check that the run has converged to a stable solution. In the left panels of Fig. 3, we plot the probability distributions inferred from each of our images separately. In the right panel, we show the product of the distributions, namely the cumulative probability distribution. The best estimate is taken to be the median of the cumulative distribution, while the 1σ uncertainty is given by the range which encloses 34.1% (total 68.2%) of the probability symmetrically on either side of the median. The offset of the ring from the stellar position in RA is in good agreement for all filters, except J-band, where it differs by half a NICI pixel (~10 mas). This is because the star was 3−5 pixels offset from the center of the mask during the J-band

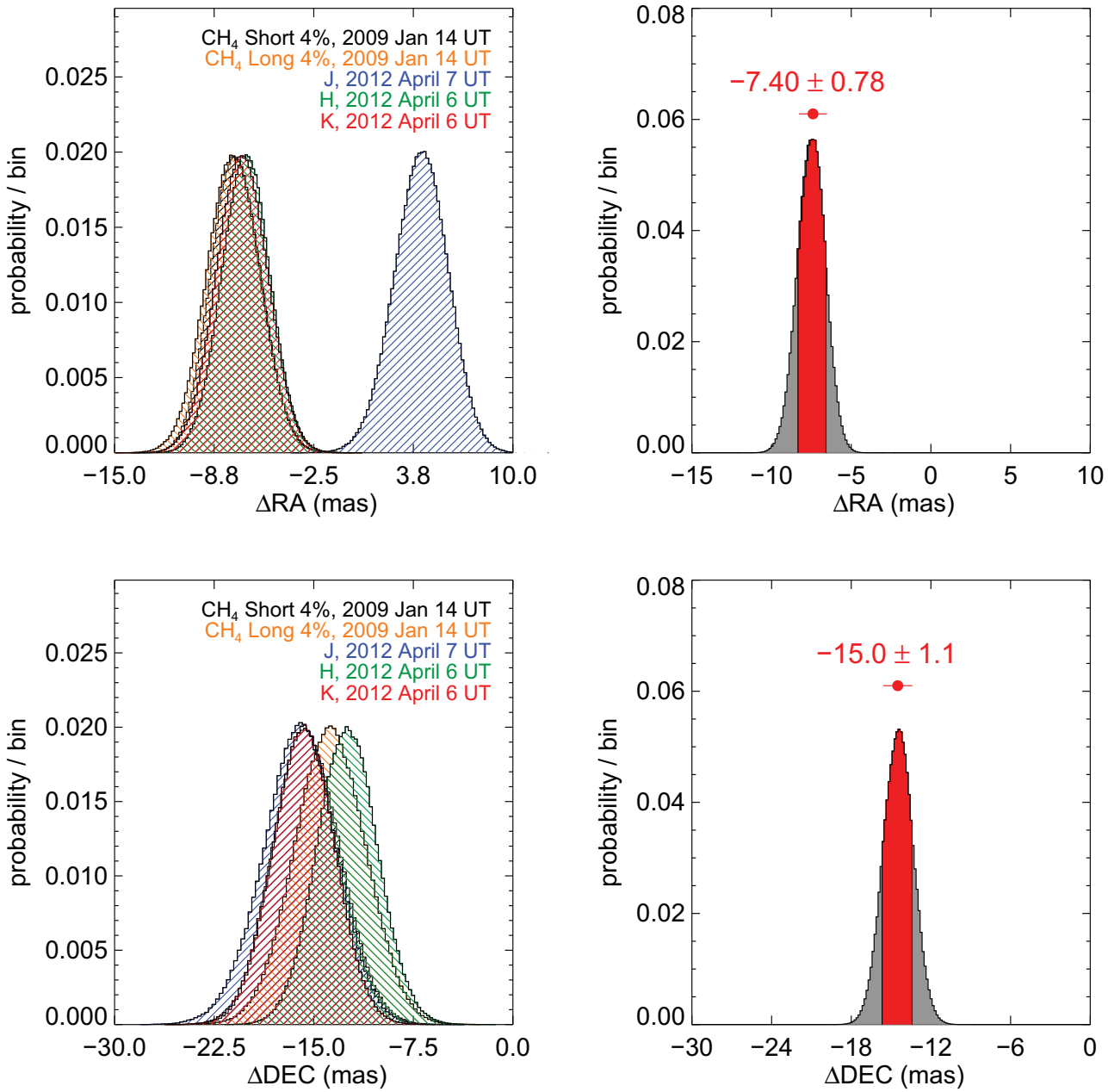

Fig. 3. *Top left*: probability distribution for the RA offset of the HR 4796 A ring for each of the 5 filters. *Right*: cumulative probability distribution with the 1σ dispersion in the distributions shown in red. *Bottom*: same for the Dec offset of the HR 4796 A ring. The offset of the ring from the stellar position in RA is in good agreement for all filters, except J-band, where it differs by half a NICI pixel (∼10 mas). This is because the star was 3−5 pixels offset from the center of the mask during the J-band observations, which likely led to a systematic error in our centroid estimate.

observations, which likely led to a systematic error in our centroid estimate. The offset of the ring in Dec is in good agreement for all five filters. The cumulative probability distributions for the two parameters show that the ring offset is 16.7 ± 1.3 mas, while the ring mean radius is estimated to be 1067 ± 2 mas. Thus the ratio of the pericenter distance to the apocenter distance is 0.969 ± 0.004 ($\frac{\text{radius}-\text{offset}}{\text{radius}+\text{offset}}$). The PA of the disk offset ($26.3 \pm 3.1°$) is roughly along the PA of the ring ($26.47 \pm 0.04°$) and the line connecting the NE and SW brightness peaks, such that the brighter ansa (NE) is closer to the star, giving credence to the idea of pericenter glow (Wyatt et al. 1999). In Fig. 4, we also see that the probability distributions for the inclination and PA of the ring are all in agreement with previous estimates of the ring properties (see Table 3), though all our new measurements are at higher precision than earlier estimates.

4.3. Method 3: modeling of self-subtraction

To investigate the possible systematic change in the ring morphology induced by self-subtraction of flux due to the ADI processing, we also tried a modified MCMC approach. In this method, each time a model image is constructed, a stack of the

Table 3. Ring offset and other properties of the HR 4796 A ring.

Ring property	This work	Schneider et al. (2009)	Thalmann et al. (2011)
ΔRA (mas)	-7.4 ± 0.8	-8 ± 4^a	-6 ± 4
ΔDec (mas)	-15.0 ± 1.1	-17 ± 4^a	-22 ± 5
$r(''$)	1.067 ± 0.002	1.057 ± 0.006	1.09 ± 0.02
PA (°)	26.47 ± 0.04	27.01 ± 0.16	26.4 ± 0.5
Inclination (°)	76.0 ± 0.07	75.9 ± 0.6	76.7 ± 0.5

Notes. [(a)] Decomposed from reported value.

model image rotated to different PAs is also constructed. These PAs are chosen to be the same as the PAs of the individual images in the real ADI sequence, as they would appear in the reference PSF used for subtraction. The median of this stack of rotated models is then subtracted from the original model to simulate the self-subtraction undergone by the reduced image. The resulting model including self-subtraction is used to compute χ^2. The MCMC method is otherwise conducted in the same way.

The results from method 3 are compared to the usual MCMC approach (method 2) in Fig. 5. The probability distributions from the two methods are in good agreement for the broad bands (total sky rotation 73° for J and 81° for H and K_s) and thus for these bands self-subtraction should not induce a large systematic error in the ring offset estimate. For the CH_4-band data (total sky rotation 24°), the two methods still yield consistent results but the difference is larger as expected given the smaller amount of sky rotation.

4.4. Comparison of the reflectivity of the dust ring in JHK_s

The observed radiation from the disk in the JHK_s bands is light scattered from the primary. If we normalize the reduced images by the primary brightness, then the relative brightnesses of the disk in the different bands represents the relative reflectivity of the disk. Should the disk be more reflective in the J-band than in the H or K_s-bands, it could indicate the presence of sub-micron grains (e.g., Fitzgerald et al. 2007; Wahhaj et al. 2007).

To better estimate the intensity of the disk, we repeat the reductions in the JHK_s-bands without applying any image filters (step 2 of the pipeline) to preserve the large-scale emission. We also choose 0.5″ wide annuli with radii of {1.8, 1.9, 2.0, 2.1, 2.2″} (in step 3) when minimizing the residuals from the PSF subtraction so as to avoid any influence of the disk. For the measurements in this section, we estimate uncertainties using the variance of measurements on the five reductions done with different annuli.

To obtain the star-to-ring brightness ratio, we correct for the focal plane mask opacity, 6.37 ± 0.12, 5.94 ± 0.05 and 5.70 ± 0.09 mag in the J, H and K_s-bands (Wahhaj et al. 2013a), respectively, by multiplying the stellar peak (observed through the mask) by $10^{0.4 \times \mathrm{opacity}}$. We then normalize the three images by the corrected stellar peak and then plot the intensity along the ring's PA as shown in Fig. 6.

The ring peak intensity H:J and K:J ratios on the SW ansa were 1.24 ± 0.03 and 1.12 ± 0.03, respectively. The H:J and K:J ratios on the NE ansa were 1.36 ± 0.03 and 1.33 ± 0.03, respectively. The trend is not clean, but the disk color seems to be redder than the primary star at least at the peak of the ring. The relative intensities of the ring are difficult to measure away from the densest part of the ring. We find that changing the radius of the fitting annulus has strong effects on the relative slopes of the ring intensity, thus making the disk colors highly uncertain away from the peak. Nevertheless, a false color image showing the reflectivity of the ring in the three bands is provided in Fig. 7.

Our ring ansae colors are consistent with Debes et al. (2008) in that the H:J and K:J intensity ratios are between 1.2 and 1.3. However, the Debes et al. (2008) NE:SW ansae brightness asymmetries in their *F110W*, *F160W* and *F222M* bands differ by upto 22% from those in our J, H and K_S bands. We should note that Debes et al. (2008) calculate total star flux using a standard star and total ring flux using aperture corrections to estimate the total reflectivity of the ring. We measure the ring to star contrast by simultaneous unsaturated imaging of both, and thus comparisons between the two color estimates are difficult. Detailed spectral modeling efforts (e.g., Debes et al. 2008; Köhler et al. 2008) to determine the chemical constituents of the dust would greatly benefit from more accurate color measurements attainable by the next generation of high-contrast instruments.

The different Strehl ratios achieved in the different bands could in principle contribute to a systematic offset in the star-to-disk brightness ratio. Fortunately, we can investigate this possibility using a known background star, 4.5″ away from the primary, which was detected as an unsaturated point source in all three bands. We deconvolve (16 iterations of Maximum Entropy) the images in each band with the corresponding point source and compare the deconvolved images by plotting the intensity profiles along the ring PA, as shown in Fig. 6. The deconvolved versions of the ring retain their star to disk brightness ratios. This indicates that the wavelength-dependent Strehl ratios do not introduce significant systematics into our measurements.

4.5. Detection limits on planetary companions

As we will discuss in the next section, there are dynamical reasons to believe that there is a planet interior to the dust ring shaping its edges. Here we calculate the sensitivity to planets on circular orbits with semi-major axes ∼ between 50−60 AU in the H-band image. To do this, we calculate the pixel to pixel rms within segments of elliptical annulli aligned with the ring, and calculate the H-band contrast limit as $(Stellar\ Peak)/(Mask\ Transmission)/(10 \times rms)$, where the mask transmission is 0.28% (Wahhaj et al. 2013a), and the stellar peak is the star's peak flux as measured through the coronagraphic mask. We checked by eye that point sources injected at the annuli location in the reduced image with peaks at 10 × (local rms) are easily discernable. The segments of the elliptical annuli are chosen to be 30 degrees wide in PA and 10 AU in radial extension, so their area in pixels correspond to about 3 NICI resolution elements. One resolution element is 3 pixels in diameter. We converted the H-band contrasts into sensitivity limits in terms of companion masses, using both COND and DUSTY models (Chabrier et al. 2000; Baraffe et al. 2003). This is because the effective temperatures of the planets of the relevant age

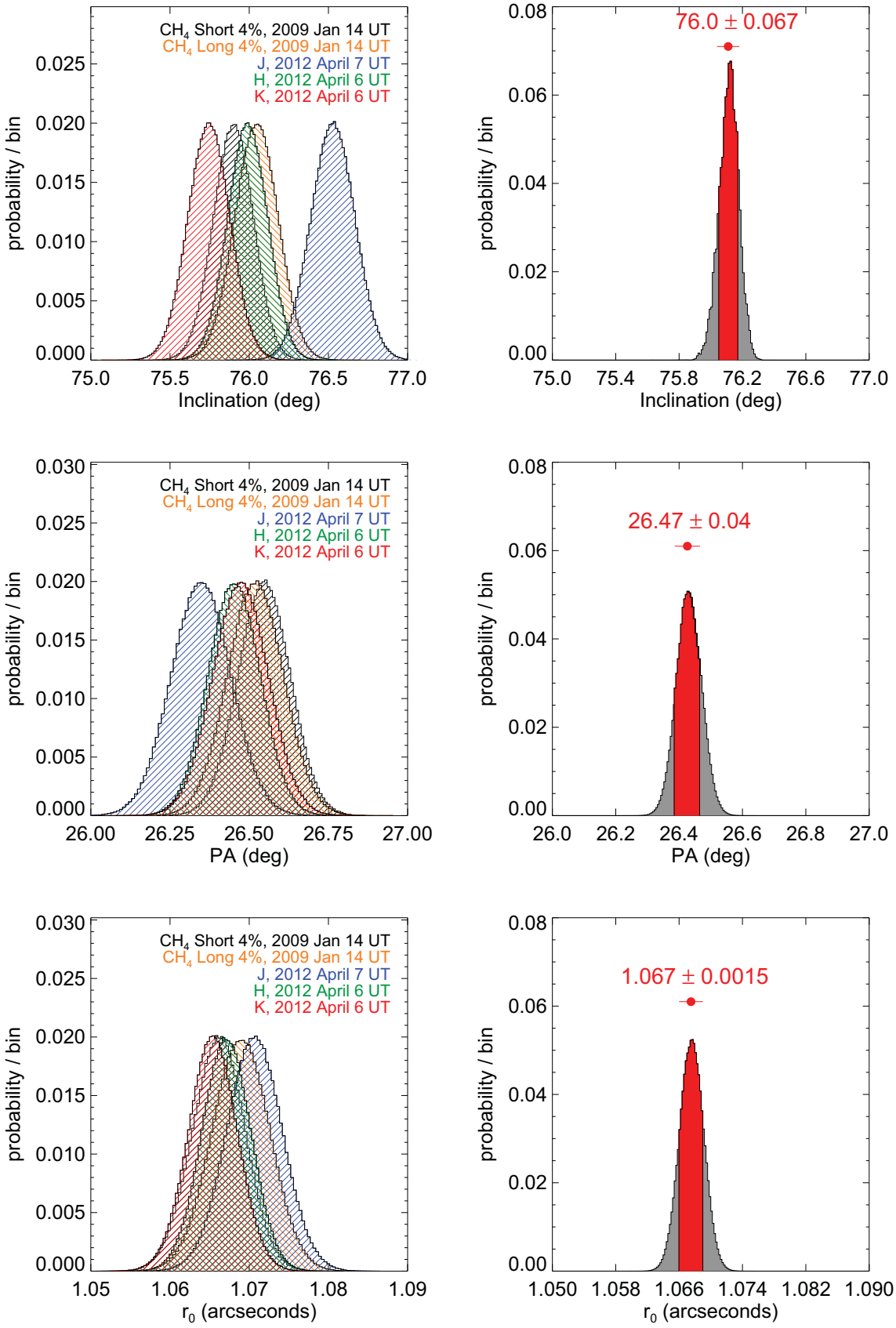

Fig. 4. Probability distributions for the other ring parameters.

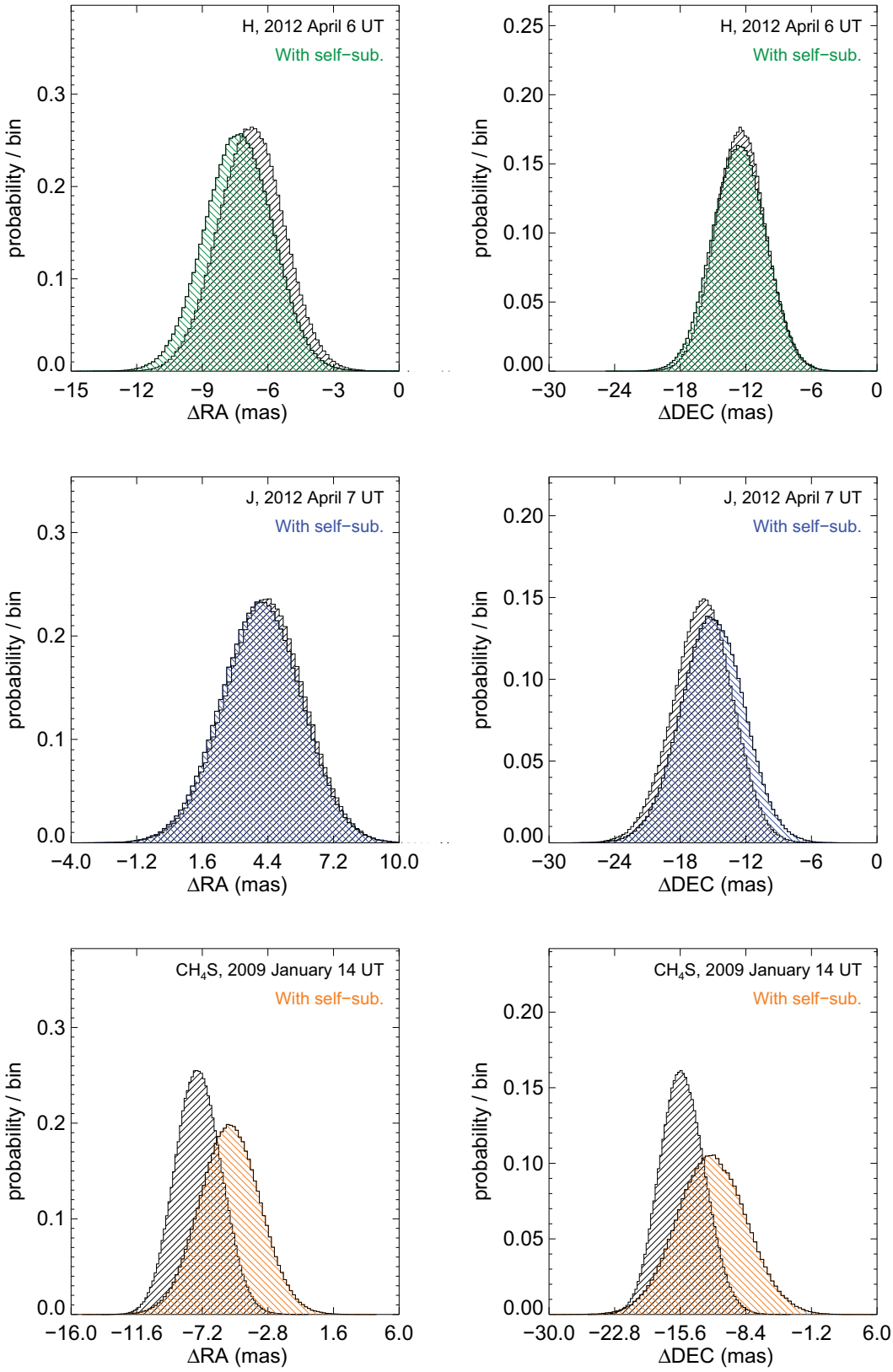

Fig. 5. Probability distributions for the *H*-band, *J*-band and CH_4 short derived ring offsets in RA and Dec for two different MCMC fitting methods. The results from the usual model comparison are shown in black (see Sect. 4.2). The results from the method where the model includes the self-subtraction (Sect. 4.3) undergone by the reduced data are shown in green, blue and orange. The offset of the ring from the stellar position in RA is in good agreement for all filters, except *J*-band, where it differs by half a NICI pixel (∼10 mas). This is because the star was offset by 3–5 pixels from the center of the mask during the *J*-band observations, which likely led to a systematic error in our centroid estimate.

Table 4. Measurements of the brightness asymmetry of the HR 4796 A ring.

SW/NE	Filter	Radiation	Reference
0.85 ± 0.02	K_s	Scattered	This work
0.78 ± 0.03	H	Scattered	This work
0.93 ± 0.02	J	Scattered	This work
0.92	0.53 μm	Scattered	Schneider et al. (2009)
0.93	1 μm	Scattered	Schneider et al. (2009)
0.6–1.0	1.10–2.22 μm	Scattered	Debes et al. (2008)
0.88	1.1 μm	Scattered	Schneider et al. (1999); Wahhaj et al. (2005)
0.93	20.8 μm	Thermal	Wahhaj et al. (2005)
0.96	24.5 μm	Thermal	Wahhaj et al. (2005)
0.77	18.1 μm	Thermal	Moerchen et al. (2011)
0.82	24.5 μm	Thermal	Moerchen et al. (2011)

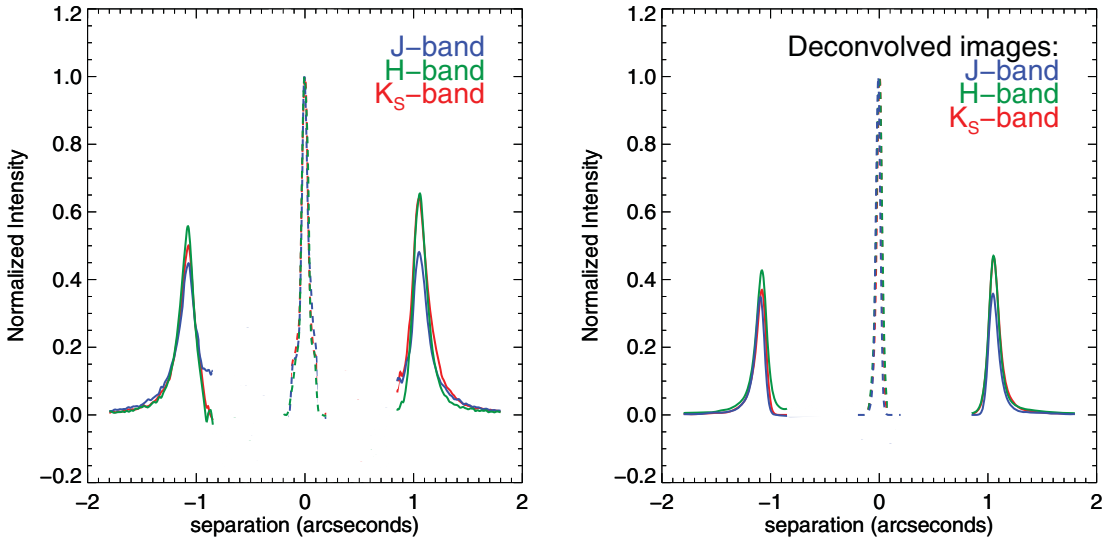

Fig. 6. *Left*: intensity profile, normalized by stellar peak, along the PA of the ring in the JHK_s-bands. The disk has roughly red reflectivity, since it is fainter in the J-band than the other two bands. *Right*: intensity profile of the deconvolved versions of the reduced images, made using a simultaneously imaged PSF star in all three bands. The relative disk colors are not significantly altered by the different Strehl ratios attained at the three wavelengths. In both plots, the dashed lines show the profiles of the stellar peak attenuated by a factor of 10 000. See Table 5 to obtain these profiles as real numbers.

and intrinsic brightnesses bracket 1400 K, a temperature below which the dust grains leave the photosphere.

We then calculate for a range of planet masses the fraction of the orbits where planets would be bright enough to be detected in our H-band image. This is then the completeness as a function of companion mass (Fig. 8). We only reach significant completeness above 8 $M_{\rm Jup}$, while only a Neptune-mass planet is required to carve the edges of the HR 4796 A ring.

4.6. Ring profile in de-projected images

In Wahhaj et al. (2005), the authors performed simultaneous modeling of the spectral energy distribution, thermal images at 12.5, 20.8 and 24.5 μm and a 1.1 μm scattered light image. They found strong evidence for both a tenuous wide and a dense narrow component to the HR 4796 A dust ring. High precision estimates were made for the inner and outer edges of the narrow component, 71.7 and 86.9 AU, with roughly 1% uncertainty for both. These distances would match the 2:1 and 3:2 resonances of a hypothetical planet at 54.7 AU. Our NICI images have less fidelity than the *Hubble* Space Telescope (HST) image used by Wahhaj et al. (2005), since HST has a much more stable PSF and the stellar light is easier to remove from the images. Thus it would not be very useful to model the NICI images without characterizing the systematic errors. Instead we simply compare the ring profile in the deconvolved and deprojected NICI images to the estimated ring edges in Wahhaj et al. (2005).

We take our deconvolved images (Sect. 4.4), and using the known inclination (76°) and PA (26°), produce the face-on appearance of the ring. This de-projected image is shown in Fig. 9 (top panel), rotated to make the NE ansa point upwards. We plot the mean intensity of the ring over the PA range −20° to +20°(in the rotated image) as a function of separation from the ring center (Fig. 9, bottom panel) and compare to the ring edge estimates in Wahhaj et al. (2005). We calculate that more than 80% of the ring flux falls within 71.7 and 86.9 AU. Thus the NICI images are also consistent with the densest part of the ring being contained within the 2:1 and 3:2 resonances of the hypothetical planet at 54.7 AU.

5. Discussion

What could be responsible for the brightness asymmetry we observe in the HR 4796 A dust ring? Since the ring-to-star distance for the NE and SW ansae have a ratio of 0.97 (NE/SW),

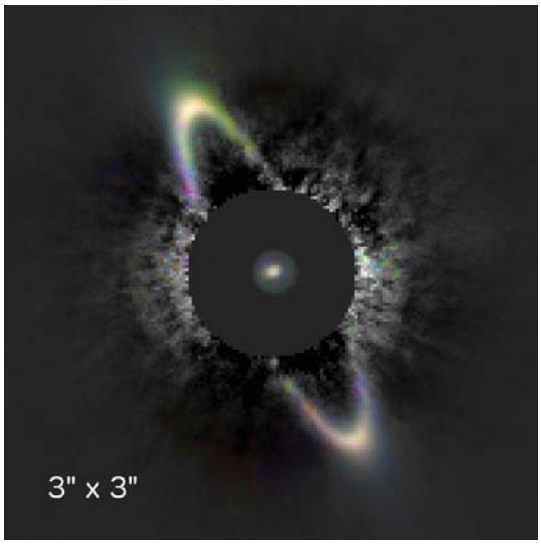

Fig. 7. A JHK_s false-color image of the HR 4796 A ring, showing its relative reflectivity, as estimated in Sect. 4.4. North is up and east is to the left. The J, H and K_s-bands are colored blue, green and red, respectively. The unsaturated star is normalized to one in all the bands and appears white in the image. The ring appears yellow because it reflects light more efficiently in the H and K_s-bands than in the J-band. The noise-dominated regions with 0.2″ to 0.5″ separation from the star are not shown. Regions away from the ring are colored white and given the median intensity of the three bands.

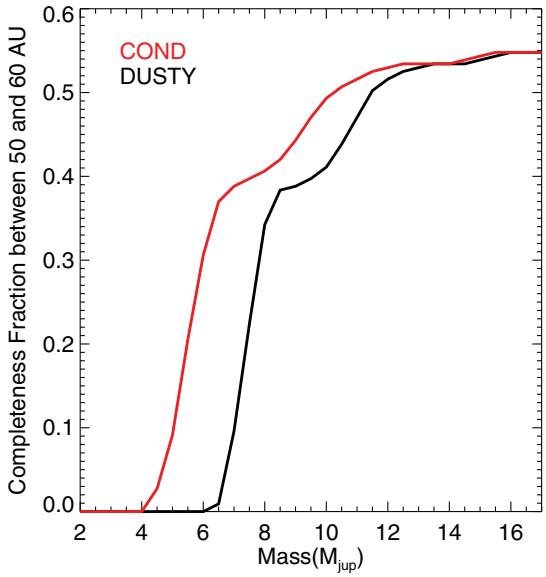

Fig. 8. Fraction of planets, as a function of mass, with orbital radii between 50–60 AU (eccentricity =0) that would be detectable in our H-band image are shown above, assuming COND (red line) and DUSTY (black line) models. The completeness does not reach 100% as some parts of the orbits are under the coronagraphic mask. Neptune-mass planets are massive enough to shape the HR 4796 A ring, but they are beyond our detection limits.

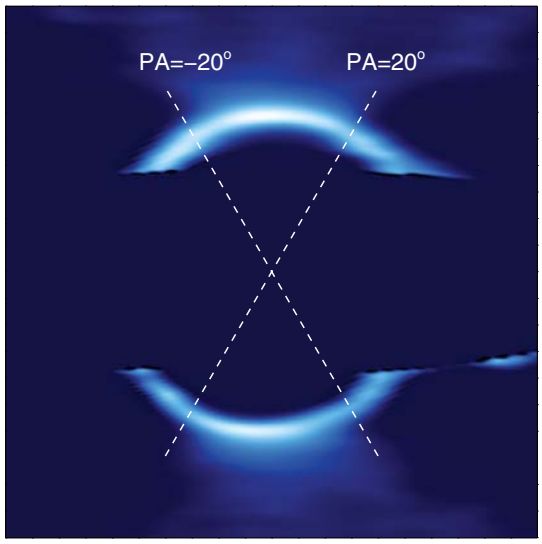

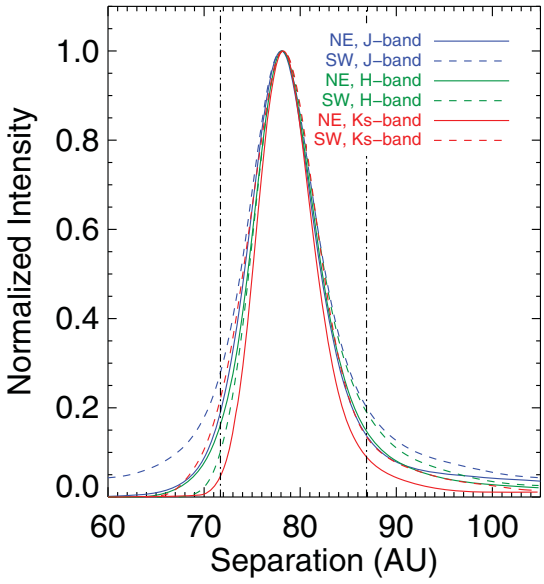

Fig. 9. *Top*: a de-projection of the deconvolved H-band reduced image, rotated to make the NE ansa point upwards. The inner, low signal-to-noise region of the ring is not shown here. Only the PA range within the two dashed lines is used to created the profiles to the right. *Bottom*: JHKs-band, normalized profiles of the deconvolved and de-projected ring, towards the NE and SW ansae, compared to the inner and outer edge estimates for the narrow-ring component in Wahhaj et al. (2005). See Table 6 to obtain these profiles as real numbers.

in scattered light the SW should be only 0.94 (=0.97^2) times as bright as the NE ansa. However, if the dust grains are on elliptical orbits, the grain density is also higher by 3% at the SW ansa, as the velocity is lower by that much at the apocenter ($\frac{\text{apocenter velocity}}{\text{pericenter velocity}} \sim \frac{\text{pericenter distance}}{\text{apocenter distance}}$ according to Kepler's laws). So we are left with a naive expectation of 0.97 (0.94/0.97) brightness asymmetry between the ring ansae. On the other hand, it is expected that higher velocities at the NE ansa will also result in a higher collision rate (Moerchen et al. 2011). The brightness asymmetry measurements in scattered light images made so far range from 0.78 to 0.93 (mean =0.88 from Table 4; note that the Debes et al. 2008 values are not included due to their large variations at similar wavelengths). Thus higher collision rates at the pericenter due to higher velocities will have to account for a further ~9% increase in asymmetry to reach the mean asymmetry of 0.88 recorded so far.

How could such a narrow asymmetric dust ring have originated? A complete dynamical model should specify the location of the generators of the dust, the planetesimals, and explain

why they are in a narrow asymmetric ring. The narrowness is important because planetesimal rings are expected to widen due to velocity dispersion (Quillen 2007). We find a possible solution in Wyatt (2003), who developed a planet migration model that is tunable to create different brightness asymmetries in exterior dust rings by mean-motion resonance trapping. The migration is necessary to capture a significant number of planetesimals into resonances. Two of the key parameters in the model are the planet to primary mass ratio and the migration rate. To match the asymmetry in a submillimeter image of Vega (which has since been refuted; see Hughes et al. 2012), Wyatt (2003) found that a Neptune-mass planet which migrated at a rate of 0.45 AU/Myr from 40 to 65 AU worked well although a range of scenarios were equally viable. HR 4796 A has a similar mass with a similar sized ring, but it is much younger. From the Wyatt et al. simulations we note that only trapping into the 2:1 resonance can create the desired asymmetry, since all other resonances produce clumps of equal brightness. Since the eccentricity of the HR 4796 A ring is only 0.032, the allowed migration is only 0.1 AU (see their Eq. (22)). Enough material needs to be present during capture and then enough time has to elapse for the primordial disk to be disperse (2−4 Myr; Wahhaj et al. 2010). Thus the capture should occur early in the life of the system (8−10 Myr; Stauffer et al. 1995). Moderate migration rates would be consistent with this scenario, say roughly 0.1 AU in 0.1−1 Myr, or 0.1−1 AU/Myr. Unfortunately, no other constrains can be obtained by considering this model since slow migration rates are consistent with both small and large planet masses. According to their Fig. 4, even a planet as small as 3 $M_{\oplus}$ would efficiently trap planetesimals into the 2:1 resonance. In any case, a specific simulation should be carried out for HR 4796 A to be check if the properties of the ring can be reproduced by this model.

The outer edge of the disk may be naturally sharp due to several reasons, although these scenarios have not yet been adequately explored by dynamical modeling: (1) only a narrow annular region is preserved by mean-motion resonance with a planet, with the rest of the disk dispersed; (2) only a narrow annular region is dynamically excited by the mean-motion resonance with the planet; or (3) very recent planetesimal break-up led to an asymmetric ring-like structure, which has not diffused yet (Jackson et al. 2014).

An interesting comparison can be made with the connection between the Kuiper belt and Neptune in the solar system. The inner and outer edges of the classical Kuiper belt coincide with Neptune's 2:1 and 3:2 resonances, respectively. This phenomenon is poorly understood but very actively studied (Levison et al. 2008; Dawson & Murray-Clay 2012). A possible explanation is that Kuiper objects were captured in resonance with Neptune as the planet migrated outward and such objects survived in larger numbers when the Kuiper belt was later cleared out by chaotic events. For HR 4796 A,Wahhaj et al. (2005) presented a single dust disk model consistent with NIR and MIR images, and photometry from MIR to millimeter wavelengths. In the model, the scattered light emission was dominated by 50 μm grains confined to a dense narrow ring, while 7 μm grains formed a tenuous wide component due to blow-out by radiation pressure and were more prominent in the MIR. Using the latest distance to HR 4796 A (72.78 pc; van Leeuwen 2007), the Wahhaj et al. (2005) estimates for the inner and outer edges of the narrow ring are updated to 71.7 and 86.9 AU, respectively. These distances correspond to the 3:2 and 2:1 resonances, respectively, of a planet at 54.7 AU to within 0.1%. However, the precision of the edge radii estimates themselves are only ∼1%. What is the probability that the edges of the ring would correspond to these resonances by chance? For such an orbital solution to exist, the ratio of the inner to outer edge radius would have to be 0.825 ($=R_{3:2}/R_{2:1} = (P_{3:2}/P_{2:1})^{\frac{2}{3}} = 0.75^{\frac{2}{3}}$) ± 0.008 (to agree to within 1%). Here $R_{2:1}$ and $P_{2:1}$ are the radius and period of the 2:1 resonance of a proposed planet, while $R_{3:2}$ and $P_{3:2}$ correspond to the 3:2 resonance. Since primordial disks typically have radii of 100–200 AU (Isella et al. 2009), the a priori expectation is that the outer radius should not be much more than twice the inner radius. Let us assume that all values of the outer radius ranging from twice the inner radius to exactly the inner radius have equal probability. Then, the probability that the inner and outer radius are by accident within 1% of the resonance solution we find is also roughly 1%. Thus the existence of a resonant orbital solution may indeed be interesting.

We also investigated if the same scenario can provide a viable explanation for the Fomalhaut debris disk, the other clearly resolved circumstellar ring system. For Fomalhaut, the highest resolution images are from Boley et al. (2012, ALMA; 870 μm), Kalas et al. (2013, HST; λ = 0.20−1.03 μm) and Acke et al. (2012, *Herschel*; 70 and 160 μm). Boley et al. (2012) made specific measurements of the ring inner and outer edges and should be considered the highest precision. The 2σ range of a Gaussian profile fit to the ring in the calibrated ALMA image was 128 AU to 155.5 AU (see their Fig. 2; right panel). For a planet with orbital radius 97.7 AU, the 3:2 and 2:1 mean-motion resonances would be at 128 AU and 155.06 AU. The ALMA image used was both de-projected and primary-beam-corrected. Kalas et al. (2013) do not specifically provide the semi-major axis of the inner and outer edges of the ring. Thus, we estimated the edge distances from their Fig. 11, an intensity map along the long axis of the ring, starting from the stellar position and binned by 20 pixels along the short axis. We estimated the edge locations where there are clear drops in intensity. The semi-major axis distances, which were calculated by dividing the measured values by (1+eccentricity), were 130 and 156.4 AU. These estimates also agree with the resonant orbital solution to within 1%. Lastly, the Acke et al. (2012) estimates, which are from a lower resolution (5.5″) image, for the semi-major axis distances were 133 and 153 AU. Given that their estimates for the mean semi-major axis of the elliptical ring has an uncertainty of 1−3 AU, their measurements are also consistent with the resonant orbit scenario.

A more general picture for the properties of planet-sculpted eccentric rings is that a planet interior to the ring clears a gap delineated by a region of overlapping mean motion resonances (Wisdom 1980) and that the orbits are collisionally relaxed (Quillen 2006). These constraints yield a unique eccentricity for the perturbing planet and a unique relationship between the planet's semimajor axis and mass. Refinements on this picture (Chiang et al. 2009; Rodigas et al. 2014) have additionally used the width of the ring to constrain the planet's mass; more massive planets tend to stir the planetesimals and dust, producing wider rings. According to the Rodigas et al. (2014) instructions for calculating a normalized FWHM for the dust ring, our *H*-band images yield a FWHM of 0.102. As we can see from Fig. 9, the ring widths in the other bands are very similar to that in the *H*-band. Our FWHM is smaller than what Rodigas et al. (2014) calculated (0.18) from previous publications on the HR 4796 A ring, probably because of better Strehl ratio in the NICI images. According to equation 5 in Rodigas et al. (2014), the planet would have to have a mass less than 2.4 $M_{\rm Jup}$ so as not to make the ring wider. Its eccentricity would be the same as that of the ring, 0.032. The maximum semi-major axis allowed

would be 51.4 AU (using Eq. (2) in Rodigas et al. 2014). But if we insist that the planet is at 54.7 AU, as in our earlier scenario, then the mass of the planet has to be less than 1.6 $M_{\rm Jup}$.

There are several alternatives to this one-planet, resonance-overlap model. Using SMACK, a modeling tool combining dynamical perturbations from a planet with collisional evolution, Nesvold et al. (2013) found that differential precession combined with collisions can play an important role in sculpting narrow rings. Or conceivably a small, stable amount of undetected circumstellar gas within the ring could be sculpting the ring via the photoelectric instability described by Lyra & Kuchner (2013). These models require deeper theoretical investigation before comparing their predictions directly with our data. Also, multiple planets might be involved in sculpting the ring, in which case there may be no unique predicted configuration for the planetary system.

6. Conclusions

We have determined that the HR 4796 A ring is offset from the star by 16.7 ± 1.3 mas based on unsaturated images in five NIR bands. These images unambiguously show the offset and confirm earlier lower-precision measurements (Schneider et al. 2009; Thalmann et al. 2011).

The densest part of the ring has a roughly red color across the $JHK_{\rm s}$ filters, indicating 1−5 μm grains (Debes et al. 2008; Köhler et al. 2008) but not 50 μm grains as in the estimates of Wahhaj et al. (2005). Away from the peak density we cannot make high precision measurements of the relative reflectivity of the ring, because of influence of the data reduction process on the wings of the ring.

We show that the brightness asymmetry of the ring in the NIR cannot be explained by the pericenter-glow effect (Wyatt et al. 1999) alone. Higher collision rates at the pericenter or some other phenomenon will have to account for 9% additional asymmetry over that provided by the pericenter glow (3%).

We discuss a possible explanation for the debris disk ring widths, which has not garnered much attention thus far. Just like Neptune's 3:2 and 2:1 mean-motion resonances delineate the inner and outer edges of the classical Kuiper belt, we find that the radial extent of the HR 4796 A and Fomalhaut rings could correspond to 3:2 and 2:1 mean-motion resonances of hypothetical planets at 54.7 AU and 97.7 AU in the two systems, respectively. For HR 4796 A we are only sensitive to planets with masses above several Jupiters. However, a planet at 54.7 AU would have to be less massive than 1.6 $M_{\rm Jup}$ so as not to widen the ring too much by stirring.

Acknowledgements. This work was supported in part by NSF grants AST-0713881 and AST-0709484. Our research has employed the 2MASS data products; NASA's Astrophysical Data System; the SIMBAD database operated at the CDS, Strasbourg, France. Facilities: Gemini-South (NICI), IRTF (SpeX).

References

Acke, B., Min, M., Dominik, C., et al. 2012, A&A, 540, A125
Backman, D. E., & Paresce, F. 1993, in Protostars and Planets III, eds. E. H. Levy & J. I. Lunine, 1253
Baraffe, I., Chabrier, G., Barman, T. S., Allard, F., & Hauschildt, P. H. 2003, A&A, 402, 701
Barrado Y Navascués, D. 2006, A&A, 459, 511
Biller, B. A., Liu, M. C., Wahhaj, Z., et al. 2013, ApJ, 777, 160
Boley, A. C., Payne, M. J., Corder, S., et al. 2012, ApJ, 750, L21
Chabrier, G., Baraffe, I., Allard, F., & Hauschildt, P. 2000, ApJ, 542, 464
Chiang, E., Kite, E., Kalas, P., Graham, J. R., & Clampin, M. 2009, ApJ, 693, 734
Chun, M., Toomey, D., Wahhaj, Z., et al. 2008, in Proc. SPIE, 7015, 1V
Dawson, R. I., & Murray-Clay, R. 2012, ApJ, 750, 43
Debes, J. H., Weinberger, A. J., & Schneider, G. 2008, ApJ, 673, L191
Fitzgerald, M. P., Kalas, P. G., Duchêne, G., Pinte, C., & Graham, J. R. 2007, ApJ, 670, 536
Gregory, P. C. 2005, Bayesian Logical Data Analysis for the Physical Sciences: A Comparative Approach with Mathematica Support (Cambridge: Cambridge University Press)
Heap, S. R., Lindler, D. J., Lanz, T. M., et al. 2000, ApJ, 539, 435
Hughes, A. M., Wilner, D. J., Mason, B., et al. 2012, ApJ, 750, 82
Isella, A., Carpenter, J. M., & Sargent, A. I. 2009, ApJ, 701, 260
Jackson, A. P., Wyatt, M. C., Bonsor, A., & Veras, D. 2014, MNRAS, 440, 3757
Jura, M., Zuckerman, B., Becklin, E. E., & Smith, R. C. 1993, ApJ, 418, L37
Kalas, P., Graham, J. R., Fitzgerald, M. P., & Clampin, M. 2013, ApJ, 775, 56
Koerner, D. W., Ressler, M. E., Werner, M. W., & Backman, D. E. 1998, ApJ, 503, L83
Köhler, M., Mann, I., & Li, A. 2008, ApJ, 686, L95
Lagrange, A., Gratadour, D., Chauvin, G., et al. 2009, A&A, 493, L21
Lagrange, A.-M., Bonnefoy, M., Chauvin, G., et al. 2010, Science, 329, 57
Lagrange, A.-M., Boccaletti, A., Milli, J., et al. 2012, A&A, 542, A40
Levison, H. F., Morbidelli, A., Van Laerhoven, C., Gomes, R., & Tsiganis, K. 2008, Icarus, 196, 258
Liu, M. C. 2004, Science, 305, 1442
Liu, M. C., Wahhaj, Z., Biller, B. A., et al. 2010, in Proc. SPIE, 7736, 1K
Lyra, W., & Kuchner, M. 2013, Nature, 499, 184
Marois, C., Lafrenière, D., Doyon, R., Macintosh, B., & Nadeau, D. 2006, ApJ, 641, 556
Marois, C., Zuckerman, B., Konopacky, Q. M., Macintosh, B., & Barman, T. 2010, Nature, 468, 1080
Metropolis, N., Rosenbluth, A. W., Rosenbluth, M. N., Teller, A. H., & Teller, E. 1953, J. Chem. Phys., 21, 1087
Milli, J., Mouillet, D., Lagrange, A.-M., et al. 2012, A&A, 545, A111
Moerchen, M. M., Churcher, L. J., Telesco, C. M., et al. 2011, A&A, 526, A34
Mouillet, D., Larwood, J. D., Papaloizou, J. C. B., & Lagrange, A. M. 1997, MNRAS, 292, 896
Nesvold, E. R., Kuchner, M. J., Rein, H., & Pan, M. 2013, ApJ, 777, 144
Nielsen, E. L., Liu, M. C., Wahhaj, Z., et al. 2013, ApJ, 776, 4
Press, W. H., Teukolsky, S. A., Vetterling, W. T., & Flannery, B. P. 1992, Numerical recipes in C. The art of scientific computing (Cambridge: University Press)
Quillen, A. C. 2006, MNRAS, 372, L14
Quillen, A. 2007, MNRAS, 377, 1287
Rameau, J., Chauvin, G., Lagrange, A.-M., et al. 2013, ApJ, 779, L26
Rodigas, T. J., Malhotra, R., & Hinz, P. M. 2014, ApJ, 780, 65
Schneider, G., Smith, B. A., Becklin, E. E., et al. 1999, ApJ, 513, L127
Schneider, G., Weinberger, A. J., Becklin, E. E., Debes, J. H., & Smith, B. A. 2009, AJ, 137, 53
Smith, B. A., & Terrile, R. J. 1984, Science, 226, 1421
Stauffer, J. R., Hartmann, L. W., & Barrado y Navascues, D. 1995, ApJ, 454, 910
Thalmann, C., Janson, M., Buenzli, E., et al. 2011, ApJ, 743, L6
Thébault, P., Marzari, F., & Augereau, J.-C. 2010, A&A, 524, A13
van Leeuwen, F. 2007, A&A, 474, 653
Wahhaj, Z., Koerner, D. W., Backman, D. E., et al. 2005, ApJ, 618, 385
Wahhaj, Z., Koerner, D. W., & Sargent, A. I. 2007, ApJ, 661, 368
Wahhaj, Z., Cieza, L., Koerner, D. W., et al. 2010, ApJ, 724, 835
Wahhaj, Z., Liu, M. C., Biller, B. A., et al. 2011, ApJ, 729, 139
Wahhaj, Z., Liu, M. C., Biller, B. A., et al. 2013a, ApJ, 779, 80
Wahhaj, Z., Liu, M. C., Nielsen, E. L., et al. 2013b, ApJ, 773, 179
Wisdom, J. 1980, AJ, 85, 1122
Wyatt. 2008, ARA&A, 46, 339
Wyatt, M. C. 2003, ApJ, 598, 1321
Wyatt, M. C., Dermott, S. F., Telesco, C. M., et al. 1999, ApJ, 527, 918

Pages 13 to 14 are available in the electronic edition of the journal at http://www.aanda.org

Table 5. Relative ring intensity profiles from the deconvolved images (from Fig. 6).

Separation (″)	J-band[a]	H-band	K_s-band
−1.8000	0.002359	0.005549	0.002596
−1.7640	0.002082	0.006486	0.002530
−1.7279	0.002077	0.006646	0.002225
−1.6919	0.002374	0.006475	0.002330
−1.6559	0.002659	0.006913	0.003002
−1.6198	0.003527	0.007517	0.004052
−1.5838	0.005002	0.007911	0.004559
−1.5477	0.005966	0.008036	0.004949
−1.5117	0.007158	0.008961	0.005808
−1.4757	0.007155	0.011643	0.006316
−1.4396	0.006545	0.014172	0.006350
−1.4036	0.008718	0.015888	0.007727
−1.3676	0.011088	0.019487	0.010773
−1.3315	0.014143	0.025478	0.015748
−1.2955	0.021652	0.033258	0.022886
−1.2595	0.032961	0.045154	0.033074
−1.2234	0.050638	0.066336	0.051993
−1.1874	0.086352	0.107026	0.088529
−1.1514	0.166844	0.187269	0.154768
−1.1153	0.304487	0.326053	0.270930
−1.0793	0.326175	0.427117	0.369613
−1.0432	0.133889	0.303743	0.229688
−1.0072	0.023503	0.131688	0.053964
−0.9712	0.001673	0.055347	0.006429
−0.9351	0.000024	0.028635	0.000322
−0.8991	0.000000	0.019321	0.000004
−0.8631	0.000000	0.017270	0.000000
−0.8270	0.000000	0.020819	0.000000
0.8090	0.000000	0.002436	0.000238
0.8450	0.000001	0.004289	0.001571
0.8811	0.000056	0.008339	0.006247
0.9171	0.001589	0.020948	0.017773
0.9532	0.021119	0.061466	0.055252
0.9892	0.125649	0.173379	0.166818
1.0252	0.317393	0.386477	0.379088
1.0613	0.337917	0.458605	0.457051
1.0973	0.203731	0.294437	0.304565
1.1333	0.103640	0.144049	0.160855
1.1694	0.053792	0.073715	0.087315
1.2054	0.030291	0.044436	0.053124
1.2414	0.018805	0.031121	0.035165
1.2775	0.012064	0.024309	0.023558
1.3135	0.009099	0.019798	0.017033
1.3495	0.008566	0.016718	0.013891
1.3856	0.007333	0.015401	0.011594
1.4216	0.006580	0.014222	0.009418
1.4577	0.006689	0.011863	0.007696
1.4937	0.006533	0.010201	0.006563
1.5297	0.005930	0.009160	0.006038
1.5658	0.004643	0.008768	0.005030
1.6018	0.003760	0.008501	0.004608
1.6378	0.004144	0.007098	0.004430
1.6739	0.003595	0.006067	0.003839
1.7099	0.002295	0.005211	0.003972
1.7459	0.002200	0.005063	0.004037

Notes. [(a)] Intensity profiles.

Table 6. Relative ring intensity profiles from the de-projected images (from Fig. 9).

Separation (AU)[a]	J-band, NE[b]	J-band, SW	H-band, NE	H-band, SW	K_s-band, NE	K_s-band, SW
59.85	0.0015	0.0432	0.0000	−0.0000	0.0000	−0.0001
60.53	0.0021	0.0445	−0.0000	−0.0000	0.0001	−0.0001
61.21	0.0026	0.0463	−0.0000	−0.0000	0.0001	−0.0001
61.90	0.0033	0.0489	0.0001	−0.0000	0.0002	−0.0002
62.58	0.0043	0.0524	0.0003	−0.0000	0.0003	−0.0006
63.26	0.0057	0.0568	0.0005	−0.0000	0.0006	−0.0007
63.94	0.0073	0.0620	0.0010	−0.0001	0.0009	0.0003
64.62	0.0096	0.0679	0.0022	−0.0001	0.0013	0.0016
65.31	0.0130	0.0750	0.0043	−0.0000	0.0017	0.0030
65.99	0.0173	0.0837	0.0070	−0.0002	0.0020	0.0066
66.67	0.0231	0.0937	0.0108	−0.0003	0.0020	0.0143
67.35	0.0311	0.1053	0.0167	0.0002	0.0020	0.0263
68.03	0.0424	0.1197	0.0250	0.0019	0.0022	0.0425
68.71	0.0576	0.1380	0.0357	0.0047	0.0032	0.0625
69.40	0.0785	0.1610	0.0495	0.0107	0.0048	0.0872
70.08	0.1072	0.1894	0.0684	0.0228	0.0091	0.1196
70.76	0.1468	0.2253	0.0948	0.0444	0.0199	0.1613
71.44	0.1990	0.2715	0.1301	0.0792	0.0427	0.2137
72.12	0.2664	0.3292	0.1765	0.1289	0.0812	0.2769
72.81	0.3497	0.3998	0.2368	0.1968	0.1429	0.3552
73.49	0.4479	0.4833	0.3173	0.2846	0.2315	0.4472
74.17	0.5624	0.5807	0.4203	0.3954	0.3500	0.5478
74.85	0.6839	0.6877	0.5412	0.5266	0.4977	0.6540
75.53	0.8011	0.7930	0.6726	0.6639	0.6568	0.7605
76.22	0.9023	0.8896	0.8000	0.7951	0.8043	0.8585
76.90	0.9709	0.9598	0.9078	0.9033	0.9187	0.9416
77.58	0.9995	0.9957	0.9788	0.9726	0.9852	0.9907
78.26	0.9828	0.9943	0.9998	0.9997	0.9978	0.9980
78.94	0.9222	0.9533	0.9730	0.9813	0.9536	0.9670
79.63	0.8338	0.8827	0.9088	0.9233	0.8630	0.9009
80.31	0.7287	0.7932	0.8202	0.8416	0.7470	0.8107
80.99	0.6230	0.6957	0.7225	0.7473	0.6216	0.7048
81.67	0.5226	0.6016	0.6217	0.6524	0.5041	0.5962
82.35	0.4318	0.5148	0.5266	0.5630	0.4000	0.4935
83.03	0.3545	0.4393	0.4426	0.4833	0.3125	0.4015
83.72	0.2909	0.3751	0.3717	0.4161	0.2421	0.3238
84.40	0.2396	0.3215	0.3128	0.3607	0.1883	0.2603
85.08	0.1986	0.2774	0.2643	0.3154	0.1490	0.2103
85.76	0.1660	0.2415	0.2250	0.2781	0.1199	0.1725
86.44	0.1404	0.2125	0.1934	0.2466	0.0976	0.1444
87.13	0.1207	0.1887	0.1683	0.2199	0.0805	0.1234
87.81	0.1055	0.1688	0.1480	0.1968	0.0678	0.1076
88.49	0.0934	0.1519	0.1314	0.1767	0.0580	0.0953
89.17	0.0838	0.1380	0.1178	0.1595	0.0499	0.0851
89.85	0.0764	0.1264	0.1068	0.1450	0.0433	0.0769
90.54	0.0706	0.1166	0.0976	0.1330	0.0380	0.0701
91.22	0.0657	0.1081	0.0897	0.1230	0.0333	0.0644
91.90	0.0617	0.1009	0.0829	0.1145	0.0291	0.0594
92.58	0.0586	0.0950	0.0770	0.1074	0.0254	0.0547
93.26	0.0562	0.0897	0.0717	0.1012	0.0223	0.0503
93.95	0.0541	0.0851	0.0669	0.0954	0.0196	0.0461
94.63	0.0523	0.0810	0.0628	0.0900	0.0174	0.0423
95.31	0.0506	0.0772	0.0591	0.0849	0.0155	0.0392
95.99	0.0491	0.0736	0.0560	0.0798	0.0141	0.0365
96.67	0.0477	0.0700	0.0533	0.0748	0.0130	0.0341
97.35	0.0463	0.0665	0.0510	0.0702	0.0122	0.0320
98.04	0.0450	0.0634	0.0491	0.0659	0.0116	0.0302
98.72	0.0437	0.0604	0.0475	0.0620	0.0112	0.0285

Notes. [a] Separation from ring center. [b] Intensity profiles.